Sansoni, Carocci & Rodella: Calibration & Evaluation of a 3-D Imaging Sensor Based on the Projection of Structured Light

Wednesday, February 10, 2021 4:15 PM

00850406

Calibration and Performance Evaluation of a 3-D Imaging Sensor Based on the Projection of Structured Light

Giovanna Sansoni, Matteo Carocci, and Roberto Rodella

***Abstract*—In this paper, the procedure developed to calibrate a whole-field optical profilometer and the evaluation of the measurement performance of the system are presented. The sensor is based on the projection of structured light and on active triangulation. The dependence of the measurements on the geometric parameters of the system is shown, as well as the criterion to calibrate the system. From the extensive set of experiments carried out to evaluate the measurement performance, good linearity has been observed, and an overall mean value of the measurement error equal to 40 μm, with a variability of about ± 35 μm has been estimated.**

***Index Terms*—Calibration, 3-D profilometry, triangulation.**

I. Introduction

RAPID, noncontact measurement methods for three-dimensional (3-D) coordinate acquisition have many applications. Typical examples are the dimensional control of the workpieces [1], and the digitization of complex, free-form surfaces in the reverse engineering and rapid product design and realization processes, where 3-D vision sensors can be successfully used, especially in conjunction with coordinate measuring machines [2].

Many techniques have been proposed, both passive and active [3]. In the active approach, scanning systems, using coherent light sources, have been accomplished [4], [5], and whole-field profilometers, based on incoherent light projection, have been developed [6]–[8]. In this frame, a number of pattern projection schemes, which differ from each other into the coding used to express the light directions, are now available. As an example, Phase Shift Methods (PSM) use real values: high resolution is achieved, even if over small measuring ranges [9]. Gray code methods (GCM) exploit integer values: the measuring range is wider than in PSM even though at the expense of reduced resolution [10]. This limitation is overcome by combining PSM and GCM, as in [11] and [12]: the addition of a fractional contribution to the integer coding of the directions of light leads to increased resolution over an extended measuring range.

A whole-field profilometer has been developed at our laboratory, based on the projection of structured light and on triangulation. An LCD projector projects bidimensional fringe patterns on the target. These patterns are acquired by a video camera and elaborated in order to obtain the range information. The approach to the coding of the light directions exploits either GCM, or PSM, and their integration into a combined procedure, called Gray Code Phase Shift (GCPS), in dependence on the required resolution and on the measuring range; the triangulation is based on the evaluation of the shift that light directions undergo in the presence of the object under measurement with respect to their position on a flat surface, which represents a reference for the measurement [13].

The integration of different light codings significantly increases the flexibility of the optical head with respect to those systems based on a single coding procedure. Actually, free-form, complex shapes can be measured by GCPS, while, for smooth surfaces, the phase methods can be exploited. Whenever an extended measuring range is required (at the expence of the resolution), GCM may be used. In general, the choice of the coding method is a tradeoff between the resolution of the measurement, the characteristics of the target shape, the whole dimension of the surface, and the time available for the projection. Moreover, a dramatic reduction of the overall measuring time is yielded by the possibility of reducing the number of different patches necessary to cover large surfaces, i.e., the possibility of guaranteeing good measuring performance even over large fields of view. This is indeed one of the objectives we worked toward, in particular for those measurements based on the GCPS method. In [12], it is shown that this can be obtained by a suitable transformation of the light codings into the spatial coordinates of the reference system used to express the measurements.

To this aim, we modeled the optical geometry of the system by three parameters: these are the distance between the projector and the video-camera, called baseline, the distance of the baseline from the reference surface, and the orientation of the projector with respect to the video-camera.

This paper presents the analysis of the height errors due to errors in the evaluation of the geometrical parameters of the model and the calibration procedure, for the accurate estimation of the triangulation parameters. Moreover, the set of measurements performed to characterize the system as far as the input-output curve, its linearity, and the variability of mean error over the whole field of view is presented. A number of experiments are also reported to highlight the flexibility of the system in the presence of objects significantly differing one from each other in both shape and dimension.

In Section II, the optical geometry is presented, and the triangulation is detailed for each coding method. The sensitivity

Manuscript received May 26, 1999; revised April 11, 2000.

The authors are with the Dipartimento di Elettronica per l'Automazione, Università degli Studi di Brescia, I-25123 Brescia, Italy (e-mail: sansoni@bsing.ing.unibs.it).

Publisher Item Identifier S 0018-9456(00)05813-7.

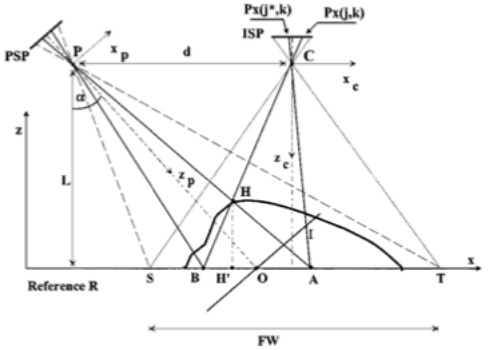

Fig. 1. Optical geometry of the system.

analysis is detailed in Section III. The procedure developed for calibrating the system is shown in Section IV. The experimental results demonstrating the effectiveness of the calibration and the performance of the system are presented in Section V.

II. Layout of the Technique

Fig. 1 shows the optical geometry of the system. The exit and entrance pupils of the projector and of the video camera are represented by points P and C respectively. The position of the optical sensors is defined with respect to reference R by baseline d and distance L. The coordinate system at the projection sensor plane (PSP) is (x_p, y_p, z_p), and that one of the image sensor plane (ISP) is (x_c, y_c, z_c): the origin is at points P and C respectively. Axes z_p and z_c coincide with the optical axes of the devices: it is assumed that z_c is perpendicular to reference R, and z_p is at angle α with respect to z_c. The depth information is defined along the z coordinate in the reference system (x, y, z). The fringes formed at PSP are parallel to y_p, and their conjugate image (with period p) is formed by the projector lens on plane I, intersecting plane R at point O. The spatial period of the fringes at reference R is p_R. Segments $\overline{PS}$ and $\overline{PT}$ represent the first and the last direction of projection seen by the video camera and define the length of field of view FW along the x-coordinate. The discrete coordinates at ISP are j and k, parallel respectively to x_c and y_c. Axes y_p, y_c and y are parallel to each other, and perpendicular to the figure plane: thus, the measured height does not depend on them and in the following they will not be considered. H is a point of the target surface, and the length of segment $\overline{HH'}$ is the height of point H, denoted in the following by z_H.

The triangulation formula used to evaluate z_H is obtained by observing that ray $\overline{PA}$ is viewed by the video-camera along the direction of acquisition $\overline{AC}$ in the absence of the object, and along the direction of acquisition $\overline{BC}$ when the object is placed on reference R. Correspondingly, at ISP, ray $\overline{PA}$ is imaged at pixel $P \times (j^*, k)$ in the absence of the object, and at $P \times (j, k)$ in the presence of the object. Height z_H is evaluated by considering that triangles $A\hat{H}B$ and $P\hat{H}C$ are similar, and that the following equation holds:

$$z_H(x, y) = \frac{L \cdot S_R(x, y)}{d + S_R(x, y)}. \tag{1}$$

In (1), $S_R(x, y)$ equals segment $\overline{AB}$ on plane R, and represents the shift that ray $\overline{PA}$ undergoes at reference R due to the object height at point $H(x, y)$. Thus, a preliminary step to the use of (1) is the evaluation of parameter $S_R(x, y)$. This step is performed by suitable light projection and coding.

A. Evaluation of $S_R(x, y)$ by Means of GCM

GCM is based on the projection at n subsequent steps, of n fringe patterns, which define in the working space 2^n directions of projection, univocally described by the words of an n-bit gray code. These patterns are acquired, binarized, and stored into a matrix, defined onto the CCD, called Bit Plane Stack (BPS). Each element (j, k) of BPS stores a code word which is then mapped to an integer number, denoted as $\hat{l}$, by using a proper look-up table. The same sequence of patterns is projected in the absence and in the presence of the object: two matrices are obtained for the reference and for the object, respectively called $\mathrm{BPS\_}R$ and $\mathrm{BPS\_}O$. Shift $S_R(x, y)$ is evaluated by means of

$$S_R(x, y) = (j - j^*) \cdot \frac{\mathrm{FW}}{N} \tag{2}$$

where N is the number of the pixels of the video camera CCD rows.

Equation (2) highlights that $S_R(x, y)$ is computed by searching, for each element (j, k) in $\mathrm{BPS\_}O$, the position (j^*, k) in $\mathrm{BPS\_}R$, where equal code number $\hat{l}$ is stored.

The univocal correspondence between the directions of projection and their codings allows the measurement of objects characterized by shape discontinuities. The binarization of the measurement area results in high repeatability of the measurement; on the other hand, the measurement resolution is rather low, due to the fact that in (2) term $(j - j^*)$ is an integer [10].

B. Evaluation of $S_R(x, y)$ by Means of PSM

PSM follows the well-known approach based on the projection of four fringe patterns of sinusoidal intensity; each pattern is obtained by spatially shifting the preceding one by a fraction $\pi/4$ of the period. The intensity fields $I_i(j, k)$ acquired in correspondence with each shift ($i = 0, 1, 2, 3$ for the considered case) are elaborated in order to determine the phase information which codifies light directions. It can be demonstrated that the following equation holds [14]:

$$\Phi(j, k) = \mathrm{atan}\frac{I_1(j, k) - I_3(j, k)}{I_0(j, k) - I_2(j, k)}. \tag{3}$$

Two phase matrices are obtained, for the reference and for the object, respectively called $\Phi_{\mathrm{Ref}}(j, k)$ and $\Phi_{\mathrm{Obj}}(j, k)$, and shift $S_R(x, y)$ is evaluated by means of the following relationship:

$$S_R(x, y) = \frac{p_R}{2\pi}[\Phi_{\mathrm{Obj}}(j, k) - \Phi_{\mathrm{Ref}}(j, k)] \tag{4}$$

where p_R is the period of the fringes at reference R. The ambiguity of the phase makes this method suitable for the mea-

surement of smooth objects; on the other hand, phase values are continuously distributed on the scene, and the resolution of the measurement is high.

C. Evaluation of $S_R(x, y)$ by Means of GCPS

GCPS can be viewed as a cascade of GCM and PSM: the last pattern of the GCM sequence is omitted; the least significant bit of the resulting, incomplete coding is computed by means of PSM; and the complete coding of the light directions is a real number, denoted by $1(j, k)$, having the following expression:

$$1(j,k) = \hat{l}(j,k) + \frac{2}{\pi}[\Phi(j,k) + \Delta\Phi(j,k)]. \quad (5)$$

In (5), $\hat{l}(j, k)$ is the integer coding obtained by the projection of the gray code sequence, $\Phi(j, k)$ is the phase value evaluated by the phase shift approach, and $\Delta\Phi(j, k)$ represents a phase correction term, experimentally evaluated.

This procedure is performed in two conditions: in the former, the patterns are projected on plane R, and (5) leads to the evaluation of a matrix, called $\mathrm{REF}(j, k)$ storing the codings corresponding to the reference plane. In the latter, the same sequence is cast on the object; the corresponding matrix is $\mathrm{OBJ}(j, k)$, and it stores the codings corresponding to the object. Shift $S_R(x, y)$ is evaluated by mapping the light codings into abscissa values along the x coordinate. This means, for the example in Fig. 1, that the abscissas x_A and x_B of points A and B are first evaluated, and then shift $S_R(x, y)$ is computed as

$$S_R(x,y) = [x_A - x_B]. \quad (6)$$

The transformation of light codings into abscissas is performed by a suitable mapping, which accounts for the mutual orientation of the projector and of the video-camera, expressed by angle α. For example, denoting with $l_{(PA)}$ the coding of ray $\overline{PA}$, the corresponding abscissa x_A is obtained by means of the following relationships:

$$x_A = L \cdot \left(\tan\left(\gamma - \operatorname{atan}\left(\frac{C_1 \cdot lp_{(PA)} \cdot \cos(\gamma - \alpha)}{1 + C_1 \cdot lp_{(PA)} \cdot \sin(\gamma - \alpha)}\right)\right)\right). \quad (7)$$

The meaning of parameters γ and C_1 is explained in Fig. 2, which represents a zoom of the projection geometry drawn in Fig. 1. In Fig. 2, T', A' and S' are the points at PSP corresponding to points T, A and S at the reference plane. Angle γ is the angle between ray $\overline{S'P}$ and the perpendicular line to reference R. It is evaluated as

$$\gamma = \tan^{-1}\left(\frac{d - \frac{\mathrm{FW}}{2}}{L}\right). \quad (8)$$

C_1 is defined as

$$C_1 = \frac{\sin(\delta_{\mathrm{tot}})}{nlp \times \sin(\theta_{\mathrm{tot}})}. \quad (9)$$

In (9), δ_{tot} and θ_{tot} are the angles shown in Fig. 2, and parameter nlp represents the total number of light codings that fall within the field of view at plane R. For a fixed configuration of the optical geometry both γ and C_1 are constant.

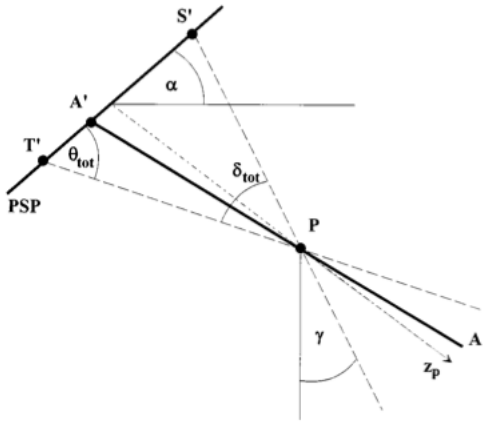

Fig. 2. Meaning of the parameters used to derive the mapping equation.

The analytical derivation of (7) is out of the scope of this paper, and the interested reader is addressed to the publication [12]. Equation (7) models the nonlinear dependence of the abscissa x_A of point A on either light coding $lp_{(PA)}$, and parameters L and α. A linear mapping, such as in (2) and (4) can not be successfully applied when GCPS is used. In fact, (2) specifically requires that the light codings are integer numbers l, while (4) can be applied only if period p_R can be considered constant at reference R. However, this hypothesis is not valid, especially for GCPS, due to 1) the crossed-optical-axes geometry of the system (points P and C are not at infinity) and 2) the geometrical setups typical of GCPS, characterized by smaller values for L and larger values for d with respect to PSM, yielding a non-negligible variation of period p_R with x-even on plane R. Thus, any attempt to evaluate shift $S_R(x, y)$ by means of (4) inherently yields an error in the estimation of the height. In [12], it has been demonstrated that this error is particularly evident on flat surfaces: the measured profile reveals a slope increasing with both x and z, and thus limits the width of the field of view. However, the entity of this error is very often negligible when PSM is used, while it must be compensated for in GCPS. The use of (7) performs this compensation, because it precisely models the relationship between the position along x of the points where the projected light rays intersect reference R and the corresponding light codings. This derivation is performed punctually, and is intrinsically insensitive to any variation of p_R.

GCPS proves to be very powerful when both extended measuring range and high resolution are required, as in the case of surfaces presenting steep slope changes and fine surface details, even for fields of view up to 400 mm × 400 mm.

III. Sensitivity Analysis

The evaluation of the object height in PSM and GCM is performed by means of (1), where only parameters L and d are involved. We suppose that small perturbations ΔL and Δd are

superimposed on nominal values L and d, respectively. The relative height error $\Delta z(x,y)/z(x,y)$ can be expressed as follows:

$$\frac{\Delta z(x,y)}{z(x,y)} = f_L\left(\frac{\Delta L}{L}\right) + f_d\left(\frac{\Delta d}{d}\right). \tag{10}$$

In (10), f_L and f_d account for the influence on the height error of the relative variations $\Delta L/L$ and $\Delta d/d$. Parameter f_L can be evaluated by the following relationship:

$$f_L\left(\frac{\Delta L}{L}\right) = \frac{z(L+\Delta L,d) - z(L,d)}{z(L,d)} = \frac{\frac{(L+\Delta L)S_R}{d+S_R} - \frac{LS_R}{d+S_R}}{\frac{LS_R}{d+S_R}} = \frac{\Delta L}{L}. \tag{11}$$

Equation (11) highlights that f_L equals 1. Parameter f_d is computed as

$$f_d\left(\frac{\Delta d}{d}\right) = \frac{z(L,d+\Delta d) - z(L,d)}{z(L,d)} = \frac{\frac{LS_R}{d+\Delta d+S_R} - \frac{LS_R}{d+S_R}}{\frac{LS_R}{d+S_R}} = -\frac{\Delta d}{d+\Delta d+S_R} \approx -\frac{\Delta d}{d}\frac{1}{1+\frac{S_R}{d}} + \left(\frac{\Delta d}{d}\right)^2. \tag{12}$$

In (12), coefficient $1/(1+(C_2L^2/d))$ is very close to 1.

If small variations of Δd are considered, (10) can be well approximated by

$$\frac{\Delta z(x,y)}{z(x,y)} = \frac{\Delta L}{L} - \frac{\Delta d}{d}. \tag{13}$$

The computation of the object height $z(x,y)$, when the coding method is GCPS, can be obtained by (1), (6), and (7); the dependence of the height error on the geometrical parameters can be expressed as the sum of three terms

$$\frac{\Delta z(x,y)}{z(x,y)} = f_L \cdot \left(\frac{\Delta L}{L}\right) + f_d\left(\frac{\Delta d}{d}\right) + f_\alpha\left(\frac{\Delta \alpha}{\alpha}\right) \tag{14}$$

where f_α accounts for the influence of angle α, and $\Delta\alpha/\alpha$ is the relative variation of α.

For simplicity, in the following the shift $S_R(x,y)$ will be expressed by the following formula, derived by combining (6) and (7):

$$S_R(x,y) = C_2 L \tag{15}$$

where C_2 is

$$C_2 = \tan\left(\gamma - \tan^{-1}\left(\frac{C_1 lp_{(PA)}\cos(\gamma-\alpha)}{1+C_1 lp_{(PA)}\sin(\gamma-\alpha)}\right)\right) - \tan\left(\gamma - \tan^{-1}\left(\frac{C_1 lp_{(PB)}\cos(\gamma-\alpha)}{1+C_1 lp_{(PB)}\sin(\gamma-\alpha)}\right)\right). \tag{16}$$

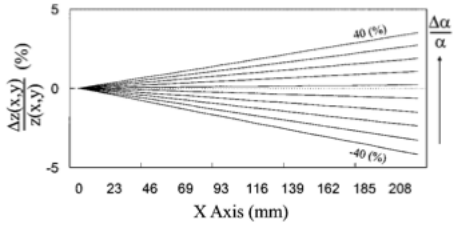

Fig. 3. Influence of $\Delta\alpha/\alpha$ on the relative height error $\Delta z(x,y)/z(x,y)$.

It has been experimentally proven that C_2 has a negligible dependence on L and, for practical purposes, can be considered constant. Combining (15) and (1) the object height is

$$z(x,y) = \frac{C_2 L^2}{d + C_2 L^2}. \tag{17}$$

Parameter f_L is derived as follows:

$$f_L\left(\frac{\Delta L}{L}\right) = \frac{z(L+\Delta L,d,\alpha) - z(L,d,\alpha)}{z(L,d,\alpha)} = \frac{\frac{C_2(L+\Delta L)^2}{d+C_2(L+\Delta L)^2} - \frac{C_2L^2}{d+C_2L^2}}{\frac{C_2L^2}{d+C_2L^2}}. \tag{18}$$

Equation (18) can be simplified if $d \gg C_2(L+\Delta L)^2$ and $d \gg C_2L^2$. This hypothesis is often verified in practice, and in this case the expression for f_L becomes

$$f_L\left(\frac{\Delta L}{L}\right) = \frac{C_2(L+\Delta L)^2 - C_2L^2}{C_2L^2} = 2\frac{\Delta L}{L} + \left(\frac{\Delta L}{L}\right)^2. \tag{19}$$

Equation (19) highlights that for small variations of L, its influence on the relative height error is linear, with coefficient equal to 2.

Parameter f_d has the same expression as in (12), already computed for GCM and PSM.

The analytical derivation of f_α is very difficult to obtain because of the high nonlinearity of (16). This dependence has been studied by means of an extensive set of numerical simulations where, for given values of parameters L, d and α, the relative height error $\Delta z(x,y)/z(x,y)$ has been computed as a function of both the relative variation $\Delta\alpha/\alpha$ and of the x coordinate. Fig. 3 shows the results for a system setup described by $L = 1192$ mm and $d = 583$ mm, and considering the variation of $\Delta\alpha/\alpha$ in the interval -40%–40%: it is well evident that, in this case, the higher x, the higher the influence of $\Delta\alpha/\alpha$ on the height error. Moreover, for a given value of $\Delta\alpha/\alpha$ the dependence of $\Delta z(x,y)/z(x,y)$ can be approximated by the following expression:

$$f_\alpha\left(\frac{\Delta\alpha}{\alpha}\right) = c_\alpha\frac{\Delta\alpha}{\alpha}x \tag{20}$$

where c_α is proportional coefficient. From the set of simulations it has been observed that this coefficient is equal to 0.55 m^{-1} with a maximum variation of $\pm 10\%$ depending on the considered set-ups. If small variations for both L and d are considered, (14) can be approximated as follows:

$$\frac{\Delta z(x,y)}{z(x,y)} = 2\frac{\Delta L}{L} - \frac{\Delta d}{d} + c_\alpha \frac{\Delta \alpha}{\alpha} x. \tag{21}$$

IV. Procedure for the Calibration of the System

The aim of the calibration procedure is the minimization of the influence of inaccuracies in the evaluation of the geometrical parameters of the system on the height error. Denoting by L_e, d_e and α_e the current estimates of parameters L, d, and α, $\Delta L = L - L_e$, $\Delta d = d - d_e$ and $\Delta \alpha = \alpha - \alpha_e$ account for these inaccuracies; the height error is expressed by (13) when PSM and GCM are considered, and by (21) if GCPS is used. In both these equations, d and L are independent parameters and, in principle, the height error can be minimized by finely varying value L_e while leaving d unchanged. Thus, the procedure does not involve parameter d, which is evaluated to the required accuracy during the setup of the system. A block of parallepipedic shape is the calibration master; its nominal height, measured by a CMM with uncertainty one magnitude order better than that one foreseen for our sensor, is z_{nom}. Denoting by z_m the profile of the master measured in correspondence with a section along the x coordinate, the exit condition of the calibration can be formulated by

$$\frac{\Delta z(L_e)}{z_{\text{nom}}} = \frac{z_m(L_e) - z_{\text{nom}}}{z_{\text{nom}}} = \frac{\Delta L}{L} < \delta z \tag{22}$$

for PSM and GCM, and

$$\frac{\Delta z(L_e, \alpha_e)}{z_{\text{nom}}} = \frac{z_m(L_e, \alpha_e) - z_{\text{nom}}}{z_{\text{nom}}} = 2\frac{\Delta L}{L} + c_\alpha \frac{\Delta \alpha}{\alpha} x < \delta z \tag{23}$$

when GCPS is considered. In (22) and (23), values L and α are obviously unknowns, and δz is the predefined tolerance within which the relative variation of the master height must be confined. The calibration procedure is based on an iterative algorithm: at each iteration, new values L_{e+1} and α_{e+1}, which estimate L and α better than L_e and α_e, are determined until the exit condition is satisfied. Values L_{e+1} and α_{e+1} can be evaluated by considering for values ΔL and $\Delta \alpha$ their approximations ΔL_e and $\Delta \alpha_e$, expressed as

$$\begin{cases} \Delta L_e = L_{e+1} - L_e \\ \Delta \alpha_e = \alpha_{e+1} - \alpha_e \end{cases} \tag{24}$$

and by substituting into (22) and (23) for nominal values L and α their estimates L_{e+1} and α_{e+1}. In this hypothesis, (22) and (23) respectively become

$$\frac{z_m(L_e) - z_{\text{nom}}}{z_{\text{nom}}} = \frac{L_{e+1} - L_e}{L_{e+1}} < \delta z \tag{25}$$

and

$$\frac{z_m(L_e, \alpha_e) - z_{\text{nom}}}{z_{\text{nom}}} = 2\frac{L_{e+1} - L_e}{L_{e+1}} + c_\alpha \frac{\alpha_{e+1} - \alpha_e}{\alpha_{e+1}} x < \delta z \tag{26}$$

for GCPS. The solution of (25) is trivial, with the term at left known from the measurement of the master height, and L_e the current estimate of L. Equation (26), instead, has two unknowns, i.e., L_{e+1}, and α_{e+1}. However, by evaluating the linear regression over $(z_m(L_e, \alpha_e) - z_{\text{nom}})/z_{\text{nom}}$, both the intercept q_e and the angular coefficient m_e can be determined, and values L_{e+1}, and α_{e+1} are retrieved as

$$\begin{cases} L_{e+1} = \dfrac{2}{2 - q_e} Le \\ \alpha_{e+1} = \dfrac{c_\alpha}{c_\alpha - m_e} \alpha_e \end{cases}. \tag{27}$$

The experimental work performed shows that typical values of convergence are 5–10 cycles, for values of δz of about 0.1% of the depth range.

V. Experimental Results

An extensive set of measurements has been performed to evaluate the performances of the system. Fig. 4 shows a photograph of the prototype used for the measurements. The projector, developed at the lab, is based on a liquid crystal panel (from CRL): it is pixel addressable, with VGA resolution. The video camera is a SONY XC-77CE, (resolution 756 × 581) equipped with the CCTV manual iris (12.5–75 mm) zoom. The acquisition and the elaboration of the images are performed by the PC Image MATRIX VISION frame grabber, with resolution $N = 800$ and $M = 2621$.

The first set of measurements relates to the determination of the system input-output characteristic curve. To this aim, a plane 300×400 mm (length × width), with height equal to 4 mm $\pm$ 0.01 mm has been chosen as a target for the measurements. It was mounted on a translation stage to explore a range along z equal to 80 mm, at steps of 4 mm each; the positioning precision of the translation stage is 0.001 mm. At each input position Z_{in} the height Z_{out}. of the target with respect to the reference has been evaluated for each point (x, y) as mean value over a set of 30 measurements. The initial estimates for angle α, and distances L and d were $\alpha_0 = 0.455$ rad, $L_0 = 1192$ mm and $d = 583$ mm, and the dimension of the illuminated area of the plane was 220 mm × 178 mm. The values determined by the calibration procedure after 14 iterations were $L_e = 1187$ mm, and $\alpha_e = 0.427$ rad. The projection sequence of GCPS has been exploited to code the light directions.

Fig. 5 shows the input-output characteristic curve of the system in correspondence with a number of test points chosen at different values of the x and y coordinates, uniformly distributed over the illuminated area. The coefficient of linear regression evaluated on the characteristic curve equals 0.9999. When the system is uncalibrated, it is characterized by a family of input-output curves, such as those plotted in Fig. 6, for increasing values of the x coordinate. Correspondingly, the

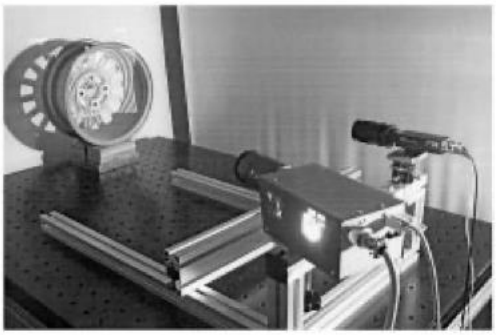

Fig. 4. Photograph of the prototype used for the measurements.

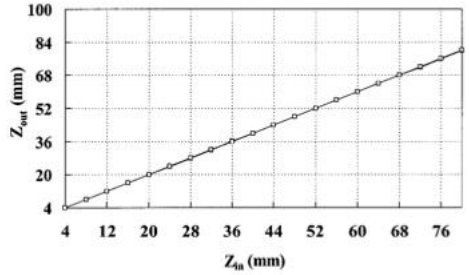

Fig. 5. Input–output characteristic curve of the system after the calibration.

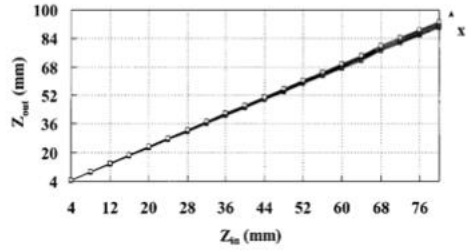

Fig. 6. Input–output characteristic curve of the system before the calibration.

measured height shows an offset, due to the inaccuracy on parameter L, and a strong dependence on both x and z, due to the inaccuracy on parameter α.

The dependence of the measurement error Δz versus Z_{in} has also been considered. To this aim we evaluated the mean value $\overline{\Delta z}$ and the standard deviation $\sigma[\Delta z]$ of the height error $\Delta z = z - Z_{\text{in}}$, where z is the height measured in correspondence with the same test points as before.f y, for increasing values along the x coordinate. The analysis demonstrated that all the parameters presented, with the exception of the measurement dispersion, do not appreciably change with both x and y. The results are shown in Fig. 7: this plot well demonstrates the ability of the calibration to bound the measurement error within a range of 12–33 μm,

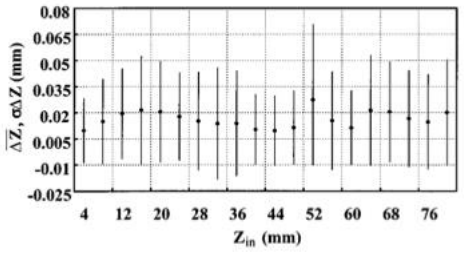

Fig. 7. Evaluation of the accuracy of the system.

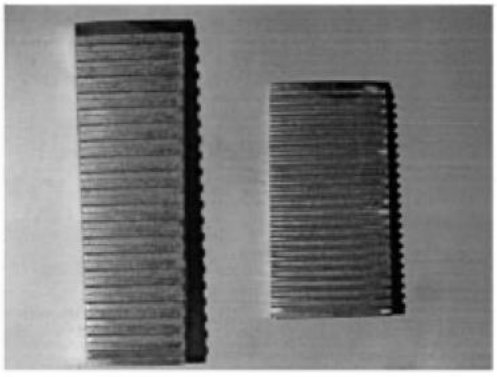

Fig. 8. Image of test objects under environmental illumination.

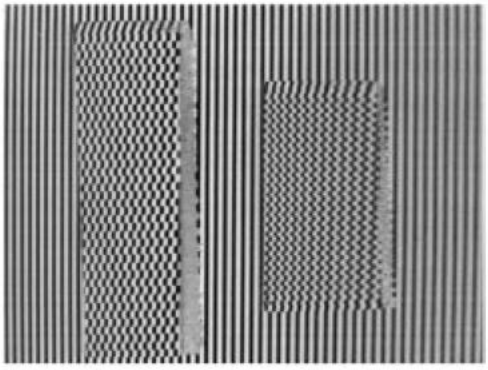

Fig. 9. Effect of the binarization of the finest fringe pattern deformed by the shape of the surfaces.

with a variability of ± 37 μm. The resulting uncertainty is 50 μm, corresponding to 0.0625% of full scale.

The characterization described so far has been extended to a number of different sets of points, chosen at fixed values o However, the mean square error $\sigma[\Delta z]$ increases by about 50% at the boundaries of the illuminated area. This is by no means surprising, considering that in these regions the quality of the

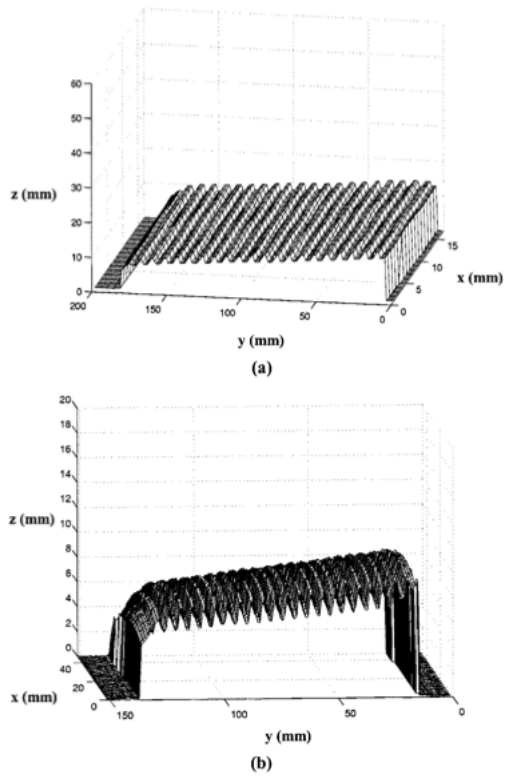

Fig. 10. Measured profiles of the objects in Fig. 8.

fringes projected decreases, both in focus and in contrast, and the influence of the lens distortion increases.

The system performance has been proven in relation with the surfaces shown in Fig. 8, characterized by regular grooves of rectangular (object at left) and triangular (object at right) profiles. The object at left is 18 mm in width and 167 mm in length, and that one at right is 25 mm in width and 110 mm in length. The optical head was set up to frame a field of view of 182 mm $\times$ 153 mm, with d equal to 280 mm, L_e equal to 503 mm, and α_e equal to 0.487 rad. The dynamic range was 60 mm. Fig. 9 depicts the fringe deformation induced by the shape of the targets on the finest pattern of the GCPS sequence, and the measured profiles are plotted in Fig. 10: here a resolution of 50 μm has been evaluated.

As an example of digitization of free-form surfaces, the measurement of the interior part of the wheel rim of Fig. 4 is reported. The complexity of shape of this object and its dimension led to a setup of the optical head characterized by larger values of L, d and α with respect to those used in the previous example, i.e., $L_e = 1283$ mm, $d = 553$ mm and $\alpha_e = 0.418$ rad; the field of view was 455 mm $\times$ 362 mm and the range in depth for this test was 150 mm. The point cloud (at reduced density) obtained (c)by means of the GCPS procedure is shown in Fig. 11(a);

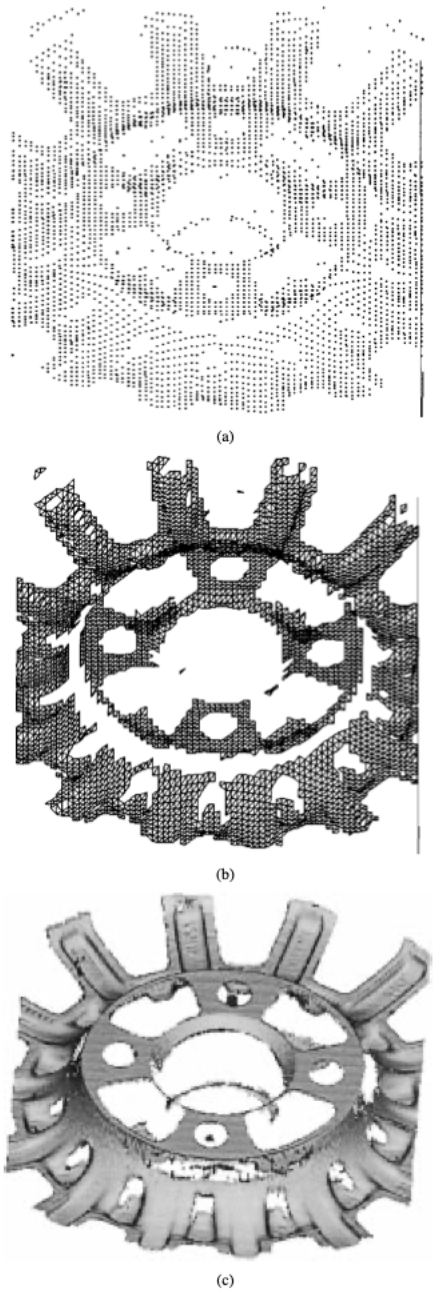

Fig. 11. Interior part of the wheel rim. (a) Acquired point cloud; (b) tessellation of the point cloud by means of triangles; (c) rendered surface.

Fig. 11(b) and (c) represent the effect of the tessellation performed by triangles of the point cloud, and the synthetic re-

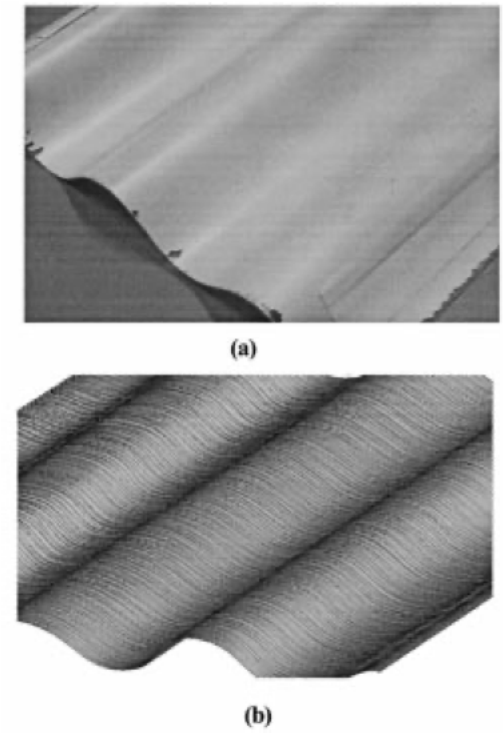

Fig. 12. Measurement of a smooth profile by means of PSM. (a) Test object; (b) measured profile.

ndering of the surface, respectively. In this measurement test, the resolution equals 70 μm, and the mean error of the measurement is within 0.1 mm, corresponding to a relative accuracy of 1/1500 of the depth range.

The last example refers to the utilization of a phase method to perform the measurement. The test object is shown in Fig. 12(a): it presents a smooth shape, which can easily be retrieved by PSM. The optimum geometry in this case was represented by $L_e = 1522$ mm, $d = 150$ mm, and $\alpha_e = 0.108$ rad, with a field of view of 367 mm $\times$ 292 mm. It is worth noting that in this setup the ratio d/L is significanly lower than in the previous examples. This is a direct consequence of the phase coding approach, which intrinsically yields high resolution, even when the projector and the camera are close to each other and distance L is large. The measured profile is shown in Fig. 12(b): here, the depth range is of about 50 mm, the resolution equals 70 μm, and the estimated accuracy is 0.1% of depth range.

VI. Conclusion

In this paper, the procedure for calibrating a whole-field optical profilometer based on the projection of structured light has been presented. The instrument integrates different approaches of light coding, in order to enhance its flexibility. The analysis of the sensitivity of the measurement to the parameters of the model is exploited to develop the algorithm for the calibration of the system: the procedure is simple, and not time consuming. An extensive set of measurements has been carried out to evaluate the measurement performance over the whole field of view, and considering objects of varied shape and dimension. The system shows high linearity and good performance for both accuracy and precision: the measurement error shows an overall mean value equal to 40 μm, with a variability of ± 35 μm. The mean error can be further reduced by considering lens distortion: to this aim, a new model for both the projector and the video-camera is under refinement and will be accounted for in future work.

Acknowledgment

The authors gratefully acknowledge the contribution of Dr. L. Rovati and Dr. S. Lazzari for their careful reading of the manuscript.

References

[1] S. F. El-Hakim and N. Pizzi, "Multicamera vision-based approach to flexible feature measurement for inspection and reverse engineering," *Opt. Eng.*, vol. 32, 1993.
[2] C. Chen and G. C. I. Lin, "An integrated reverse engineering approach to reconstructing free-form surfaces," *Comput. Integr. Manufact. Syst.*, vol. 10, no. 1, pp. 49–60, 1997.
[3] R. A. Jarvis, "A perspective on range finding techniques for computer vision," *IEEE Trans. Pattern Anal. Machine Intell.*, vol. PAMI-5, no. 2, pp. 122–139, 1983.
[4] M. Rioux, "Laser range finder based on synchronized scanners," *Appl. Opt.*, vol. 23, pp. 3837–3843, 1984.
[5] A. M. McIvor, "Calibration of a laser stripe profiler," in *Proc. 2nd Int. Conf. 3-D Digital Imaging and Modeling*, 1999, pp. 92–98.
[6] D. M. Meadows, W. O. Johnson, and J. B. Allen, "Generation of surface contours by moiré patterns," *Appl. Opt.*, vol. 9, pp. 942–947, 1970.
[7] L. Pirodda, "Shadow and projection moiré techniques for absolute or relative mapping of surface shapes," *Opt. Eng.*, vol. 21, pp. 640–649, 1982.
[8] S. Kuwamura and I. Yamaguchi, "Wavelength scanning profilometry for real-time surface shape measurement," *Appl. Opt.*, vol. 36, pp. 4473–4482, 1997.
[9] V. Srinivasan, H. C. Liu, and M. Halioua, "Automated phase-measuring profilometry: A phase mapping approach," *Appl. Opt.*, vol. 24, pp. 185–188, 1985.
[10] G. Sansoni, S. Corini, S. Lazzari, R. Rodella, and F. Docchio, "3-D Imaging based on Gray code light projection: Characterization of the measuring algorithm and development of a measuring system for industrial applications," *Appl. Opt.*, vol. 36, pp. 4463–4472, 1997.
[11] W. Krattenthaler, K. J. Mayer, and H. P. Duwe, "3D-Surface measurement with coded light approach," *Proc. Öesterr. Arbeitsgem. MusterErKennung*, vol. 12, pp. 103–114, 1993.
[12] G. Sansoni, M. Carocci, and R. Rodella, "3D vision based on the combination of gray code and phase shift light projection: Analysis and compensation of the systematic errors," *Appl. Opt.*, vol. 36, pp. 6565–6573, 1999.
[13] G. Sansoni, M. Carocci, S. Lazzari, and R. Rodella, "A 3D imaging system for industrial applications with improved flexibility and robustness," *J. Opt. A: Pure Appl. Opt.*, vol. 1, pp. 83–93, 1999.
[14] M. Carocci, S. Lazzari, R. Rodella, and G. Sansoni, "3D range optical sensor: Analysis of the measurement errors and development of procedures for their compensation," *Proc. SPIE, Three-Dimensional Image Capture*, vol. 3023, pp. 139–147, 1998.

Giovanna Sansoni received the degree in electronic engineering from the Politecnico of Milan, Milan, Italy, in 1984.

She is now Associate Professor at the Department of Electronics for the Automation of the University of Brescia, Brescia, Italy, and responsible for the research activity of the Imaging Group at the Lab. of Optoelectronics of the department. Her main research interests are in the area of 3-D vision. Since 1986, she has been working at a number of research projects covering different fields, such as the development of advanced interferometric systems exploiting heterodine detection at multiple frequences for absolute distance measurement; implementation of camera and projector calibration for the absolute measurement of shape in active stereo vision systems; development of light coding methods for whole-field optical profilometry.

Matteo Carocci received the M.S. degree in electronic engineering from the University of Brescia, Brescia, Italy, in 1997. His M.S. thesis, entitled "3-D measurement procedure based on integration of grey-code and phase-shift projection: analisys of the the systematic errors and development of algorithm for their compensation," was developed at the Laboratory of Optoelectronics, with the supervision of Prof. G. Sansoni and Ing. S. Lazzari. In 1998, he joined the Department of Industrial Automation (now the Department of Electronics for the Automation) at the same university, where he is currently pursuing the Ph.D. degree in electronic instrumentation.

Roberto Rodella received the degree in electronic engineering from the University of Brescia, Brescia, Italy, in 1996. In 1998, he spent a research period at the Visual Information Technology Group, IIT, NRC, Ottawa, Ont., Canada, and, in 1999, he received the Ph.D. degree in information engineering from the University of Brescia.

His research interest is in the development and characterization of optoelectronic systems and devices for surface inspection and 3-D measurement. In particular, he has been involved in projects for the application of the 3-D noncontact measurement techniques in the industrial and cultural heritage fields for metrology, quality control, reverse engineering, rapid prototyping, and virtual reality.